Supplementary Information (SI) for Green Chemistry.
This journal is © The Royal Society of Chemistry 2026

Supplementary information

Component Modulation Strategy of Waste Camellia Shell via Hydrogen Bond Competition within Neutral Deep Eutectic Solvent to Construct Hard Carbon as High-Performance Sodium-Ion Battery Anode

Jiaying Chen [1], Xi Yu [1], Yuejin Zhan [1], Jing Huang [2], Hanlin Hu [1], Bi Luo [1*], Hui Li [2], Ping Gao [3], Yefeng Zhou [1*]

[1] National & Local United Engineering Research Centre for Chemical Process Simulation and Intensification, College of Chemical Engineering, Xiangtan University, Xiangtan, 411105, China.

[2] State Key Laboratory of Woody Oil Resources Utilization, Hunan Academy of forestry, Changsha, 410004, China

[3] Key Laboratory of Enviromentally Friendly Chemistry and Application of Ministry of Education, College of Chemistry, Xiangtan University, 411105 Xiangtan, China

[*] Email of the corresponding author: zhouyf@xtu.edu.cn (Y. Zhou); biluo@xtu.edu.cn (B. Luo).

1 Experimental Section

1.1 Reagent sources

Camellia shells were sourced from Jiazhiyuan Tung Oil Workshop in Jiangxi Province. N-methylpyrrolidone (AR) and choline chloride (AR, 98%) were acquired from Shanghai Aladdin Reagent Co. Hydrochloric acid, ethanol, and ethylene glycol (AR) were obtained from Sinopharm Chemical Reagent Co., Ltd. Ultrapure water (18.25 MΩ·cm^{-1}) was generated using a water purification system (YL-100, Shenzhen Yiliyuan Water Treatment Equipment Co., Ltd., Shenzhen, China).

1.2 Preparation of materials

Preparation of raw materials: The camellia shells were initially washed with ethanol and deionized water, followed by ultrasonication at room temperature for 1 h and drying at 80 °C. The dried shells were then ground using a pulverizer and sieved through a 100-mesh screen to obtain camellia shell powder. Deep eutectic solvent (DES) was prepared by mixing choline chloride and ethylene glycol at a 1:2 molar ratio under magnetic stirring at 80 °C for 2 h, yielding a uniform transparent solution.

DES pretreatment: 40 wt% deionized water was added to the prepared DES and thoroughly mixed. Camellia shell powder and DES were then added to the solution at a mass ratio of 1:10, followed by stirring in a constant-temperature water bath at 80°C

for 0 h, 0.25 h, 0.50 h, and 0.75 h, respectively. After the reaction, solid residues were separated by centrifugation, alternately washed with deionized water and ethanol until the liquid became clear, and dried at 80 °C for 12 h to obtain the pretreated biomass samples. PHC-X specifically refers to the solid intermediate product of camellia shell obtained after pretreatment with neutral DES for different durations (X = 0, 0.25, 0.50, 0.75 h). In addition, the liquid samples collected after DES treatment for 0 h, 0.25 h, 0.50 h, and 0.75 h are designated as DES-0, DES-0.25, DES-0.50, and DES-0.75, respectively.

Pyrolysis: The precursor material treated with DES for 0.5 h was pyrolyzed at 1100 °C, 1200 °C, 1300 °C, and 1400 °C, and the resulting hard carbon materials were designated as HC-0.50-1100, HC-0.50-1200, HC-0.50-1300, and HC-0.50-1400. The precursors treated with DES for 0 h, 0.25 h, 0.50 h, and 0.75 h were subsequently carbonized at 1200 °C for 2 h to obtain the final hard carbon products, labeled as HC-X, where X represents the DES treatment duration.

1.3 Electrochemical Characterization

The slurry was prepared by mixing hard carbon (90 wt%), Super C65 (5 wt%), and polyvinylidene fluoride (PVDF) (5 wt%) in N-methyl-2-pyrrolidone (NMP). The slurry was cast onto a copper foil, dried at 110 °C for 12 h, and then cut into 12-mm-diameter anode electrodes (mass loading: 2-3 mg). The cells (CR2032) were assembled in a dry glove box filled with argon (O_2 < 0.01 ppm). Metallic sodium and a glass-fiber separator (GF/C) were employed as the counter electrode and separator, respectively. About 100 μL electrolyte (1 M $NaPF_6$ in diethyl ether) was injected in to the cell.

Electrochemical measurements were conducted with a LAND battery test system (Wuhan, China) and a Princeton Versa STAT 4 electrochemical workstation. A rate of 1 C was defined as 300 mA h g^{-1}. Cyclic voltammetry (CV) tests were performed between 2.5 and 0.01 V at scan rates ranging from 0.1 to 1.0 mV s^{-1}. Electrochemical impedance spectroscopy (EIS) was measured from 100 kHz to 0.01 Hz with a 5 mV amplitude voltage. For galvanostatic intermittent titration technique (GITT) experiments, the cells were discharged at 0.1 C for 20 min, followed by a 30 min rest, then a 0.1 C charge for 20 min and another 30 min rest.

2. Materials Characterization

The NREL method [1, 2] for determining the three main components. The phase structure of the biochar was characterized using X-ray powder diffraction (XRD, Smart Lab SE, Rigaku, Japan) with Cu Kα radiation (λ = 0.15405 Å) at a scanning speed of 10 °min^{-1} over a 2θ range of 10-90 °. The surface morphology of the hard carbon materials was examined with a high-resolution field-emission scanning electron microscope (FE-SEM, Sigma 30, ZEISS, UK). Specific surface area and pore-size distribution were measured by Brunauer-Emmett-Teller (BET) analysis (Micromeritics ASAP 2460, USA). Compositional and structural information was obtained via confocal Raman spectroscopy (Renishaw in Via, Thermo Fisher Scientific, USA) employing a 532 nm laser and scanning from 500 to 3500 cm^{-1}. Surface chemical bonds/functional groups were identified by Fourier-transform infrared spectroscopy (FTIR, Nicolet 6700, Thermo Fisher Scientific, USA). Elemental composition, content, and valence states were analyzed using elemental analysis (EA, Elementar Vario EL III, Germany) and X-ray photoelectron spectroscopy (XPS, Thermo Scientific K-Alpha, USA).

3. Correlated Calculations

The crystallinity index: The CrI is calculated by the Siegel peak height method, and the equation is as follows [3].

$$Crystallinity\ index(CrI) = \frac{I_{200} - I_{AM}}{I_{200}} \times 100 \quad \text{(S1)}$$

Where the peak intensity of the (200) reflection (I_{200}) at 2θ = 22°-23° corresponds to the combined signal of crystalline and amorphous materials. The intensity minimum near 18°, located between the (110) and (200) peaks, represents the amorphous region. Its measured intensity (I_{AM}) quantifies the amorphous content.

NREL method [1, 2] for determining the three main components. The specific operational procedure is as follows:

A total of 300 mg of the extracted and dried camellia shells (m_0, g, oven-dry) was transferred into a 10 mL centrifuge tube. Next, 3 mL of 72% sulfuric acid was added and shaken well, then hydrolyzed in a water bath at 30 ℃ for 1 h. The hydrolysate was

transferred to a 100 mL conical flask, 84 mL of ultrapure water was injected and weighed. The resulting mixture was sealed, sterilized (121 ℃, 1 h), filtered, and the filtrate pH was adjusted to 1 to 3. The concentrations of glucose (C_{glu}, mg/mL), arabinose (C_{ara}, mg/mL), and xylose (C_{xyl}, mg/mL) were determined by high-performance liquid chromatography (HPLC). Substituting them into Equation S2 and S3, respectively, **the content of cellulose (C, %) and hemicellulose (H, %) in corn stalk can be calculated:**

$$C(\%) = \frac{C_{glu} \times 87 \times 10^{-3} L \times 0.90}{m_0} \times 100 \quad \text{(S2)}$$

$$H(\%) = \frac{(C_{xyl} + C_{ara}) \times 87 \times 10^{-3} L \times 0.88}{m_0} \times 100 \quad \text{(S3)}$$

Determination of acid-insoluble lignin content:

The residue obtained from two-step acid hydrolysis was washed with hot distilled water until the filtrate was neutral. It was placed in an oven at 105 ℃ for constant weight, m_1 (g), and then carbonized, burned in a muffle furnace at 575 ℃ for 4 h, cooled and weighed, m_2 (g). The content of acid-insoluble lignin in corn stalk was calculated by Equation S4:

$$L(\%) = \frac{m_1 - m_2}{m_0} \times 100 \quad \text{(S4)}$$

Determination of acid-soluble lignin content:

A small amount of hydrolysate was taken, and its absorbance at 320 nm was measured with a DR6000 ultraviolet spectrophotometer to determine the content of acid-soluble lignin (ASL, %). The calculation formula is shown in Equation S5,

$$ASL(\%) = \frac{UV \times V \times n}{\varepsilon \times m \times P} \times 100 \quad \text{(S5)}$$

where UV is optical density, V is volume of hydrolysate (mL), m is the hydrolysate weight (g), n is the dilution ratio, Ɛ is the absorption coefficient (25 L $(g \cdot cm)^{-1}$), and P is the color plate thickness (cm).

Cellulose-to-Lignin ratio:

$$\frac{Cellulise}{Lignin} = \frac{C(\%)}{L(\%)} \times 100 \quad \text{(S6)}$$

The average width (L_a): The length of the graphitic domains along the lateral ab

direction (L_a) can be estimated using the following formula [4].

$$L_a(nm) = (2.4 \times 10^{-10})\lambda_{nm}^4(I_G/I_D) \quad \text{(S7)}$$

where λ_{nm} is the laser wavelength (532 nm), and I_G and I_D are the intensities of the G-band and D-band.

The $d_{(002)}$ value: The average interlayer d-spacing could be determined according to Bragg's equation [5].

$$d = \frac{\lambda}{2sin\theta} \quad \text{(S8)}$$

where d is the average interlayer spacing, n is the diffraction order, θ is the diffraction angle, and λ is the X-ray wavelength (Cu Kα radiation, λ = 1.5405 Å).

The closed pore volume：

$$V_{closed\ pore} = \frac{1}{\rho_{ture}} - \frac{1}{2.26} \quad \text{(S9)}$$

where ρ_{ture} is true densities of hard carbon materials. The value of 2.26 g cm^{-3} is derived from the true density of graphite, considered an ideal crystal with no closed pore structure [6].

The values of a and b: The value of b can be calculated from the slopes of log (*i*) versus log (*v*), which are indicative of the contribution of Na storage mechanisms. A value of b close to 0.5 suggests that the electrochemical reaction is primarily diffusion-controlled, while a value of b close to 1.0 indicates that capacitance-controlled behavior dominates [7].

$$i = av^b \quad \text{(S10)}$$

$$\log i = \log a + blog\ v \quad \text{(S11)}$$

where *i* and *v* represent the peak current and scan rate

The relative contributions of **capacitance-controlled** and **diffusion-controlled** processes in CV curves can be further quantified by equation [8].

.

$$i = k_1V + k_2V^{\frac{1}{2}} \quad \text{(S12)}$$

where V represents the scan rates, k_1V and $k_2V^{1/2}$ denote the contributions of capacitance-controlled and diffusion-controlled capacity.

The Na diffusion coefficient (D_{Na+}): The semicircle in the medium-to-high-frequency region is composed of the contact resistance (R_s) and the charge-transfer resistance (R_{ct}), and the inclined line in the low-frequency region corresponds to the Warburg impedance [9].

$$\omega = 2\pi f \quad (S13)$$

$$Z'' = R_s + R_{ct} + \sigma\omega^{-\frac{1}{2}} \quad (S14)$$

$$D = 0.5R^2T^2/S^2n^4F^4C^2\sigma^2 \quad (S15)$$

ω and σ denote the angular frequency in the low-frequency region and the Warburg impedance coefficient, R represents the gas constant (8.314 J mol^{-1} K^{-1}), T signifies the absolute temperature (293.15 K), S stands for the electrode surface area, n denotes the number of electrons per mole of active material involved in the electrochemical reaction process, F indicates the Faraday's constant, C represents the Na molar concentration.

Diffusion coefficient of sodium ion (D_{Na+}): The diffusion coefficient of sodium ion (D_{Na+}) can be estimated by Fick's second law equation [10].

$$D_{Na+} = \frac{4}{\pi\tau}\left(\frac{m_B V_m}{M_B S}\right)^2\left(\frac{\Delta E_s}{\Delta E_t}\right)^2 \quad (S16)$$

in which τ represents the pulse duration, m_B and S are related to the active mass loading and surface area of the electrode, V_M and M_B refer to the molar volume and weight of the active material, ΔE_s and ΔE_t (refer to voltage variation led by galvanostatic charge/discharge and pulse, respectively) can be acquired from the GITT curves.

4. Simulation Parameters

Since cellulose, lignin, and hemicellulose are all high-molecular-weight polymers, performing full-atom density functional theory (DFT) calculations is computationally infeasible. Therefore, we used representative model compounds to construct the computational models. Firstly, we established molecular models for DES and the three biomass components. Hemicellulose model: The structural unit is shown in **Figure S4(a)**, with a degree of polymerization of 3. Cellulose model: The structural

unit is shown in **Figure S4(b)**, with a degree of polymerization of 2. The lignin model adopted an irregular conformation as shown in **Figure S4(c)**, constructed with a 6:3:1 ratio of guaiacyl, syringyl, and p-hydroxyphenyl units. After establishing the molecular models, we performed geometric optimization on the DES and the three biomass component molecules to obtain the lowest energy and most stable structures. Subsequently, we conducted studies on properties such as energy, electron density, electrostatic potential, and population analysis, ultimately obtaining the results for electrostatic potential and binding energy.

Geometric optimization and property calculation parameters: Precision set to Fine, exchange-correlation functional to GGA-PBE, energy convergence to $1.0*e^{-5}$ Ha, max. force to 0.002 Ha $Å^{-1}$, max displacement to 0.005 Å, max iterations to 1000, max. step size to 0.3 Å. In Electronic parameters, SCF tolerance set to $1.0*e^{-6}$, max. SCF cycles to 1000. To accelerate convergence, "use smearing" was enabled with a smearing value of 0.005 Ha. Other parameters were set to the software defaults.

4. Results

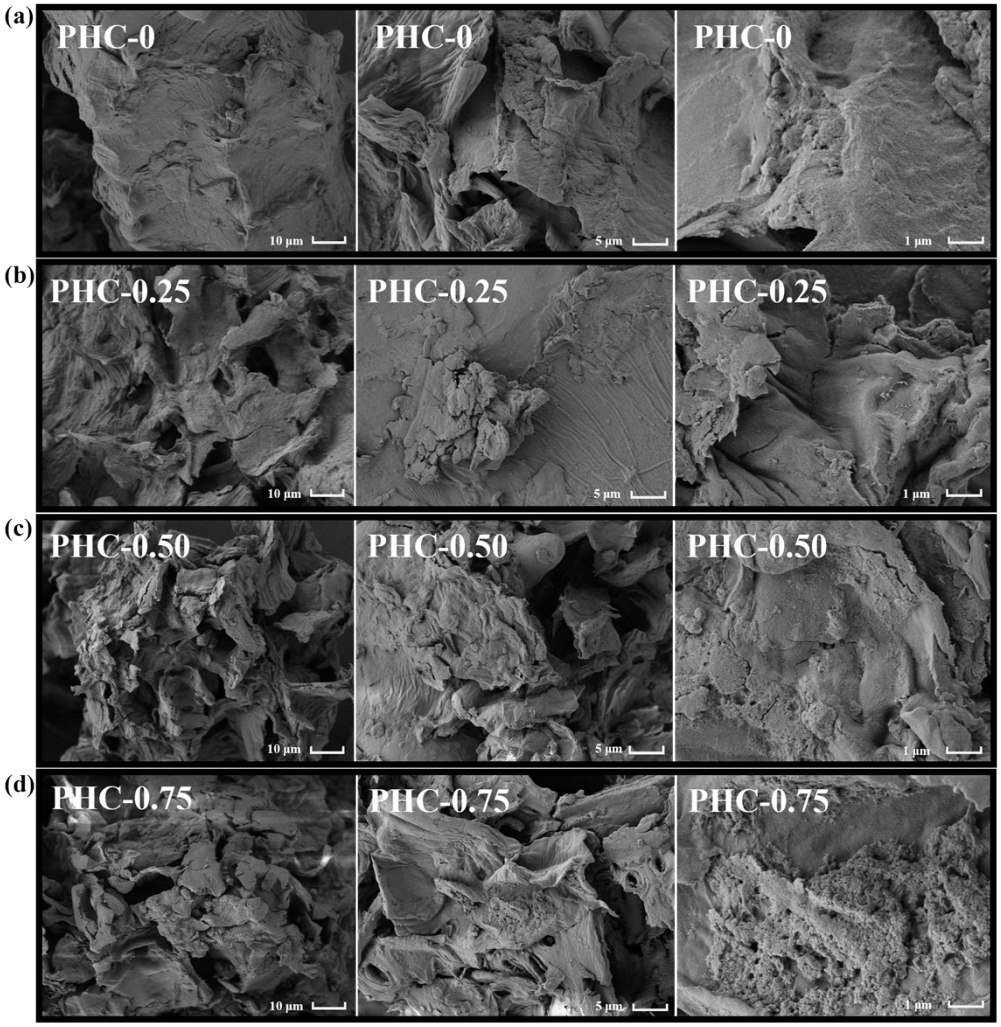

Figure S1. SEM images of (a) PHC-0, (b) PHC-0.25, (c) PHC-0.50, (d) PHC-0.75.

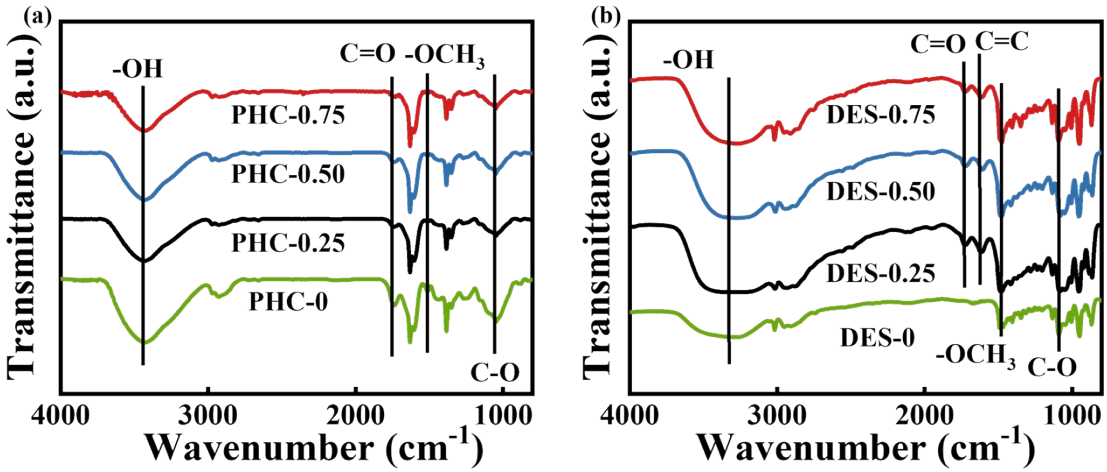

Figure S2. (a) FT-IR spectra of PHC-X, (b) FT-IR spectra of DES-X.

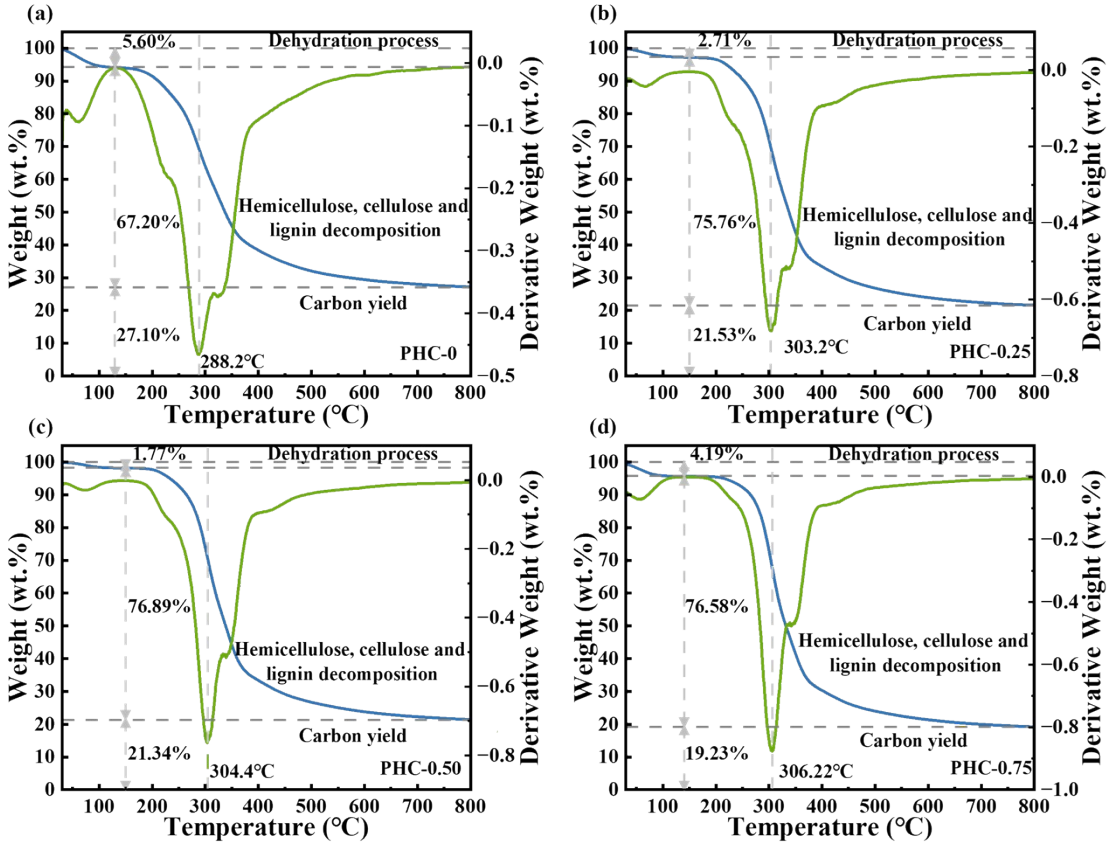

Figure S3. TG and DTG curves in a nitrogen atmosphere of (a) PHC-0, (b) PHC-0.25, (c) PHC-0.50, and (d) PHC-0.75.

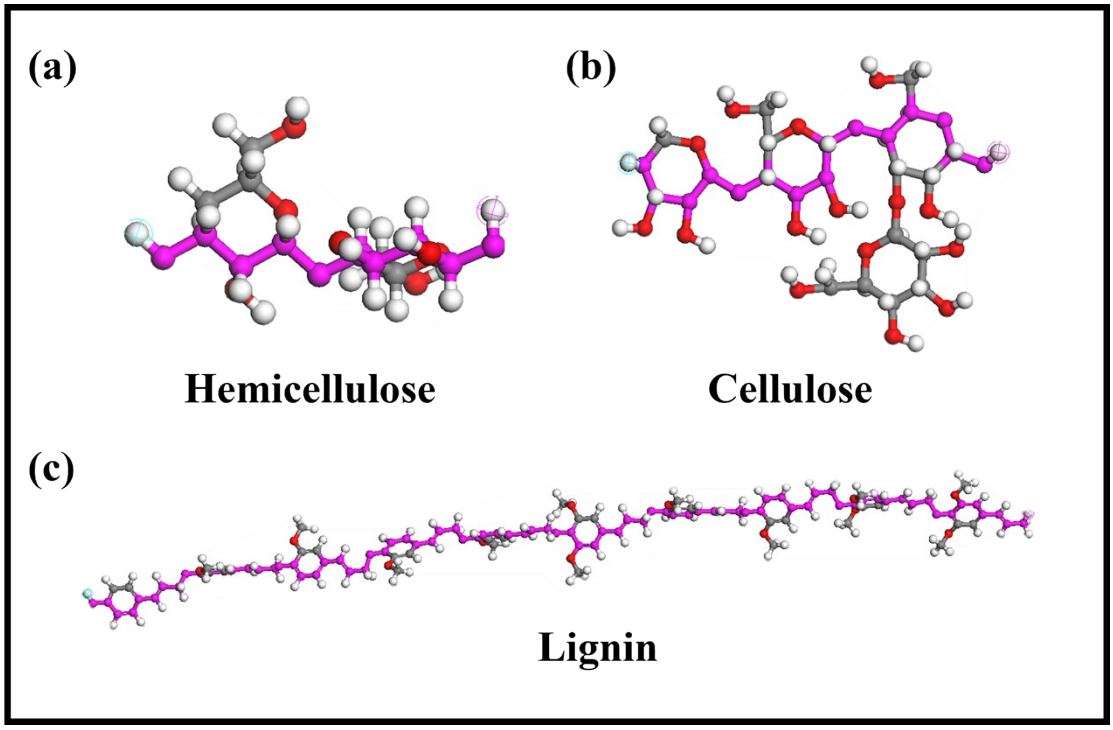

Figure S4. Monomer structural models of (a) Hemicellulose, (b) Cellulose, (c) Lignin.

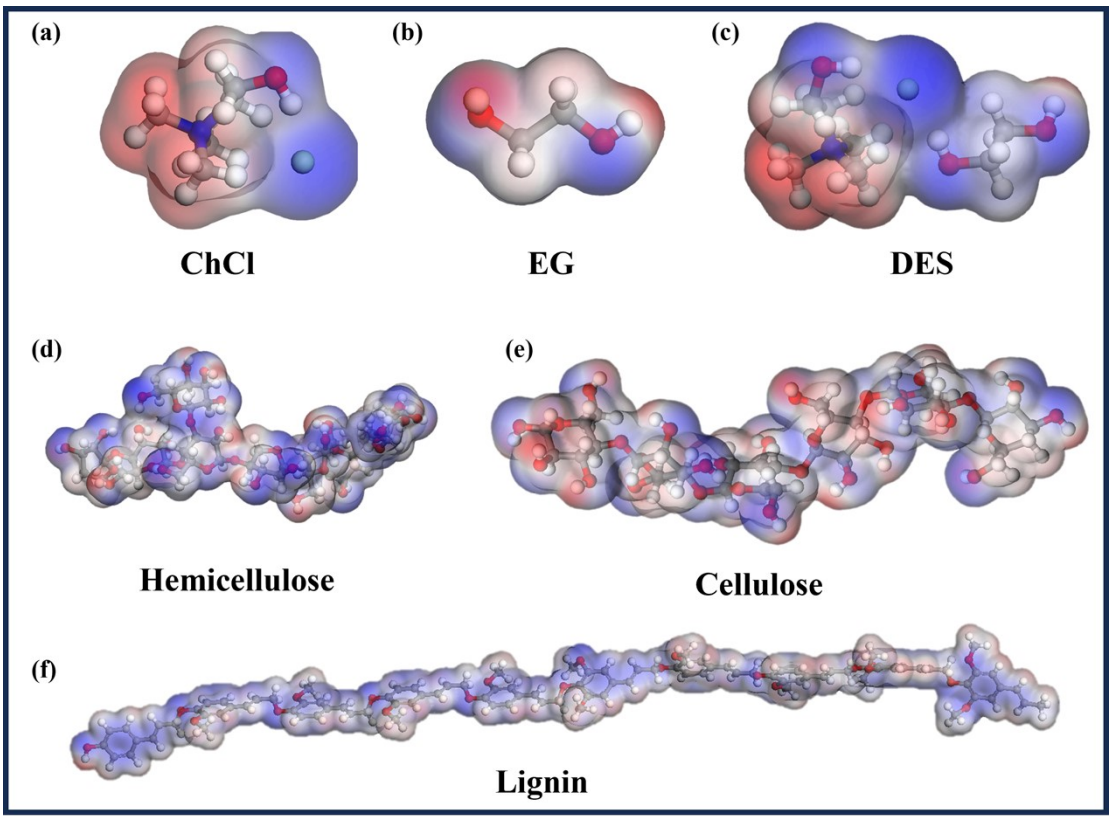

Figure S5. Molecular structure and electrostatic potential map of (a) ChCl, (b) EG, (c)DES, (d) Hemicellulose, (e) Cellulose, (f) Lignin.

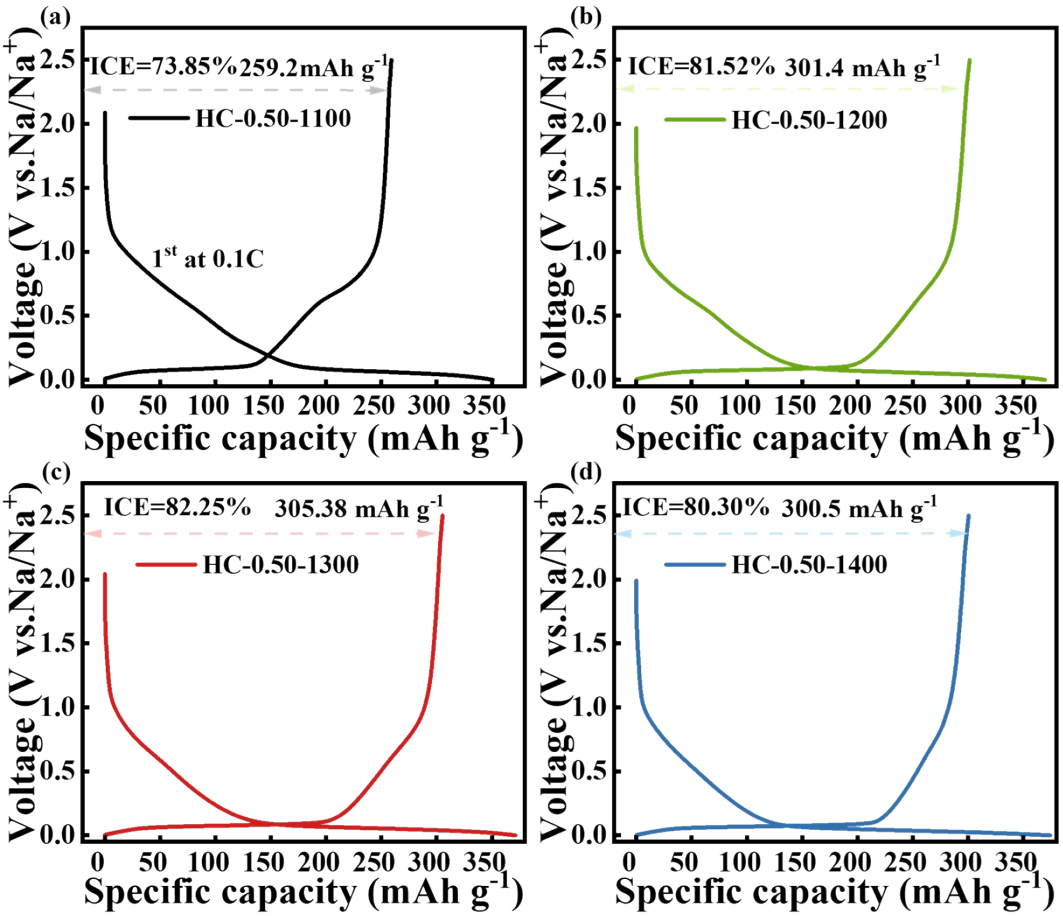

Figure S6. Initial galvanostatic charge/discharge at 0.1 C of (a) HC-0.5-1100, (b) HC-0.5-1200, (c) HC-0.5-1300, (d) HC-0.5-1400.

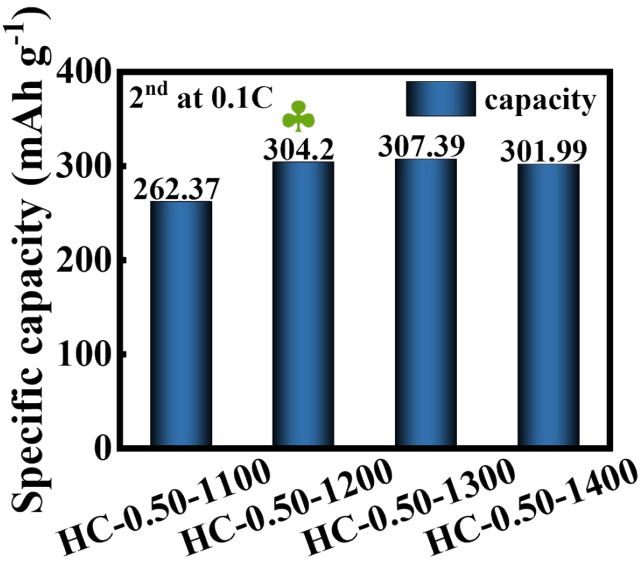

Figure S7. Plateau and slope capacity contribution.

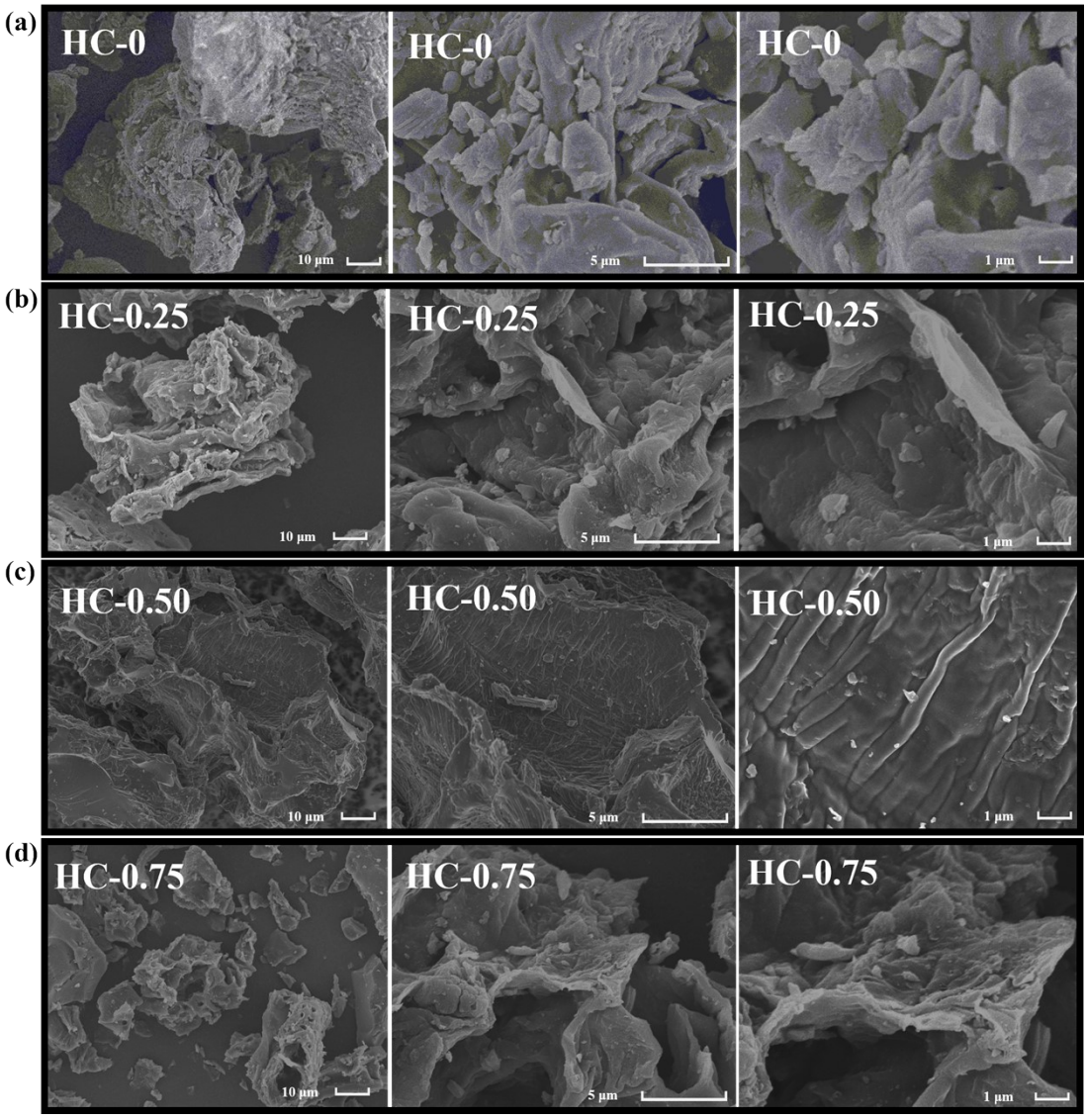

Figure S8. SEM images of (a) HC-0, (b) HC-0.25, (c) HC-0.50 and (d) HC-0.75.

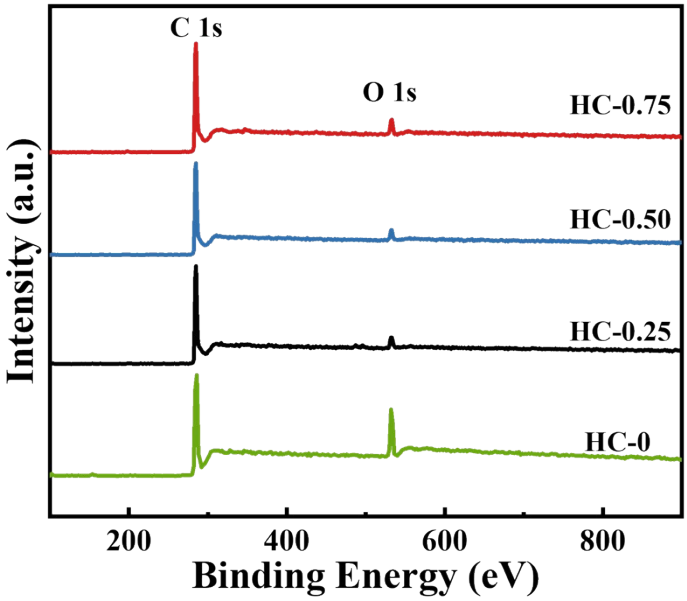

Figure S9. XPS surveys of HC-X.

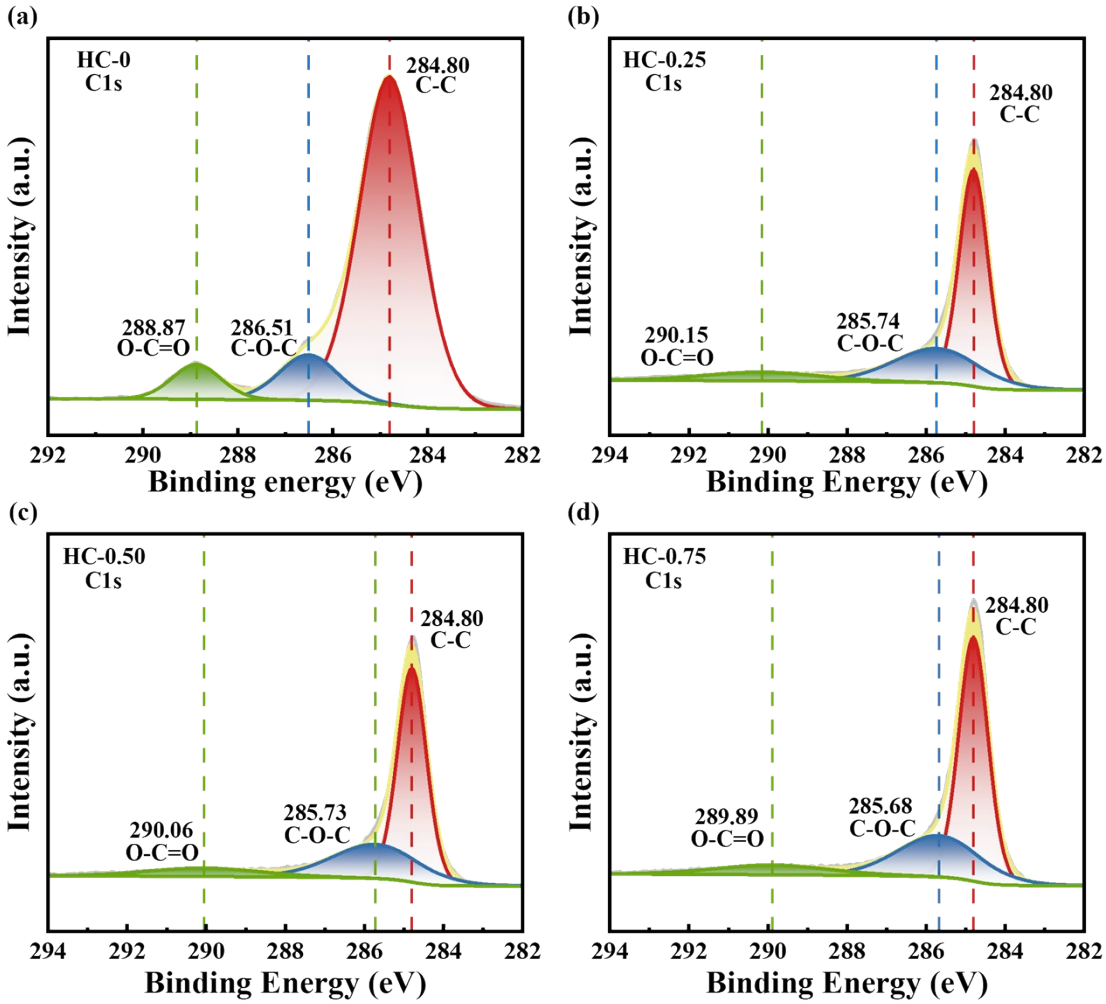

Figure S10. The high resolution of C1s peak fitting profiles for (a) HC-0, (b) HC-0.25, (c) HC-0.50, and (d) HC-0.75.

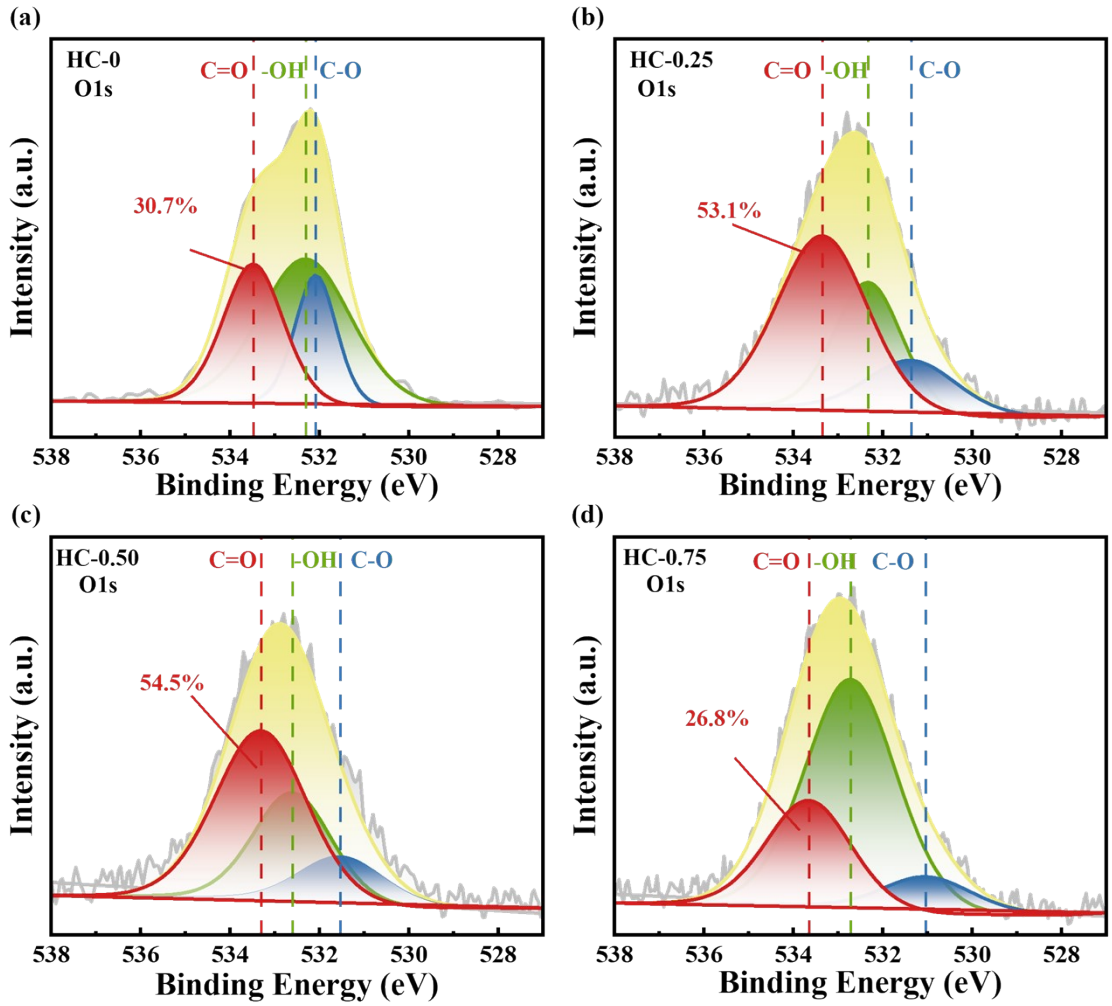

Figure S11. The high resolution of O1s peak fitting profiles for (a) HC-0, (b) HC-0.25, (c) HC-0.50, and (d) HC-0.75.

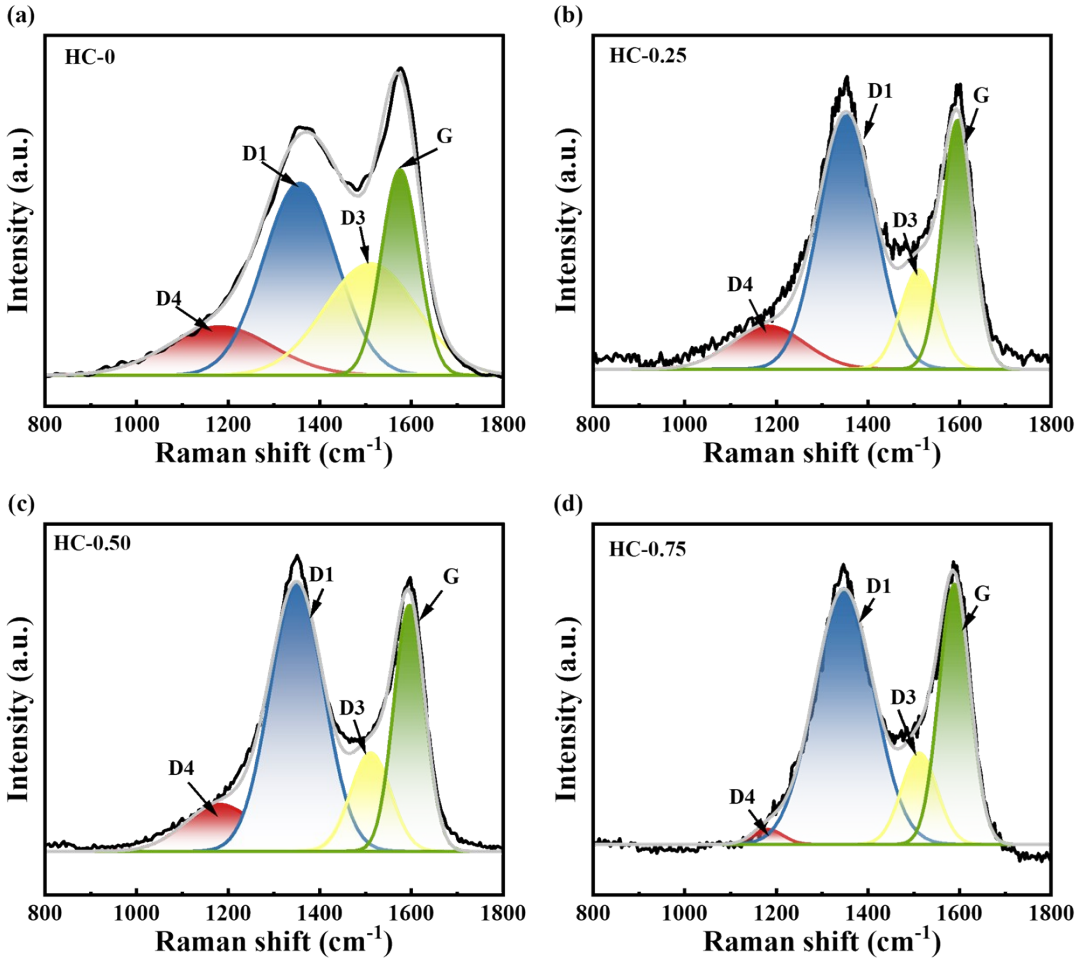

Figure S12. Peak fitting of the Raman spectra: (a) HC-0, (b) HC-0.25, (c) HC-0.50, (d) HC-0.75.

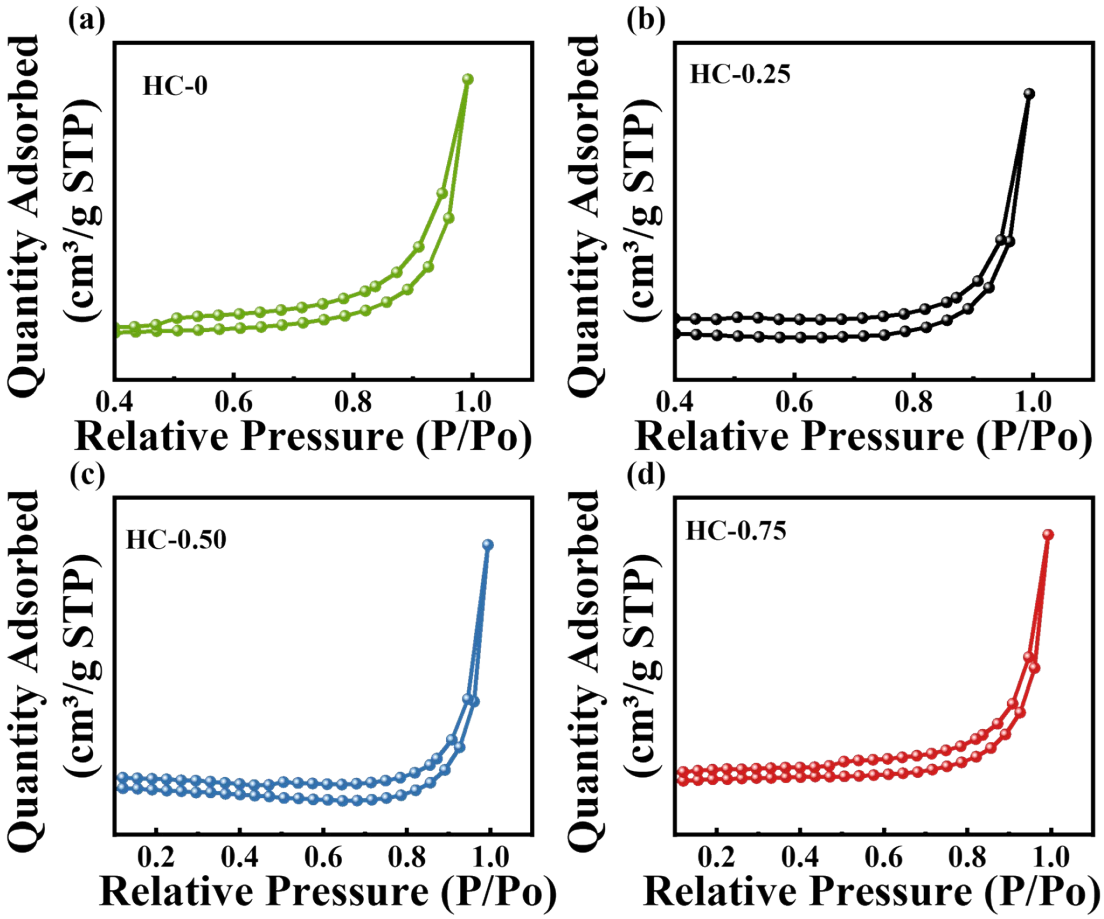

Figure S13. N_2 adsorption-desorption isotherms of (a) HC-0, (b) HC-0.25, (c) HC-0.50, (d) HC-0.75.

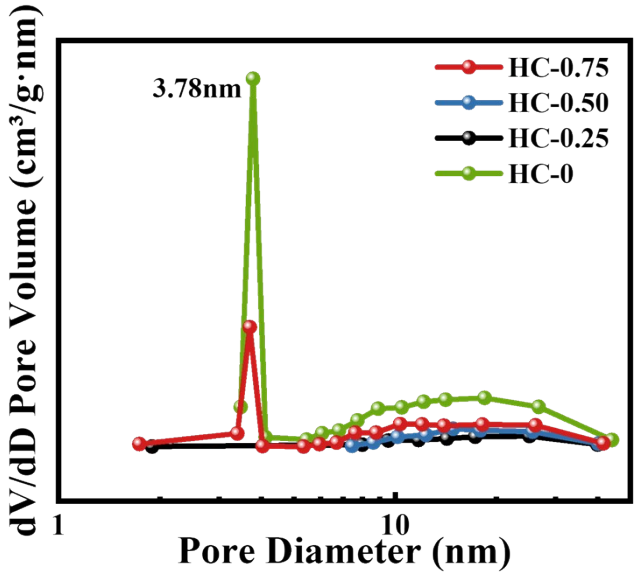

Figure S14. Pore size distribution of HC-X.

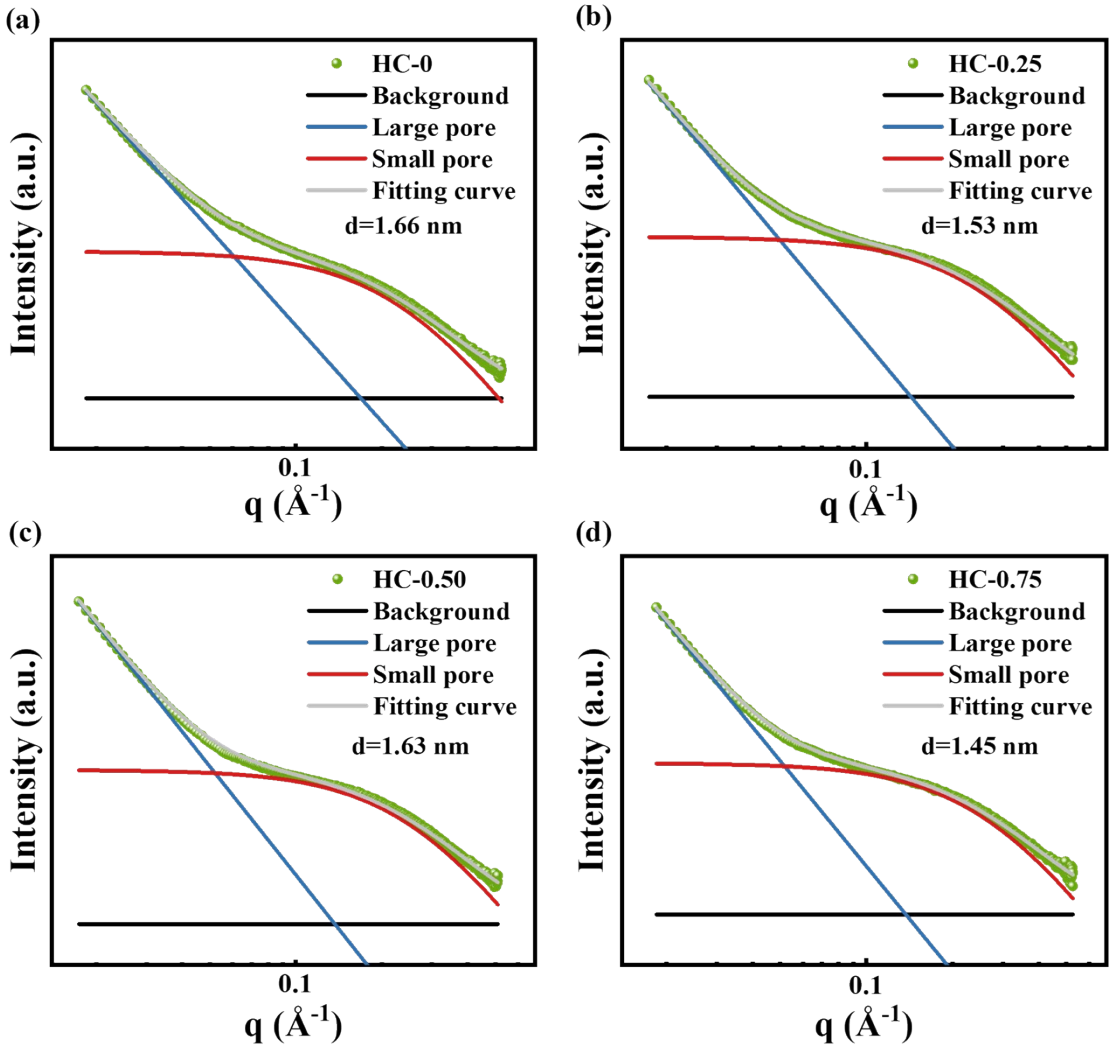

Figure S15. Fit SAXS pattern of (a) HC-0, (b) HC-0.25, (c) HC-0.50, (d) HC-0.75.

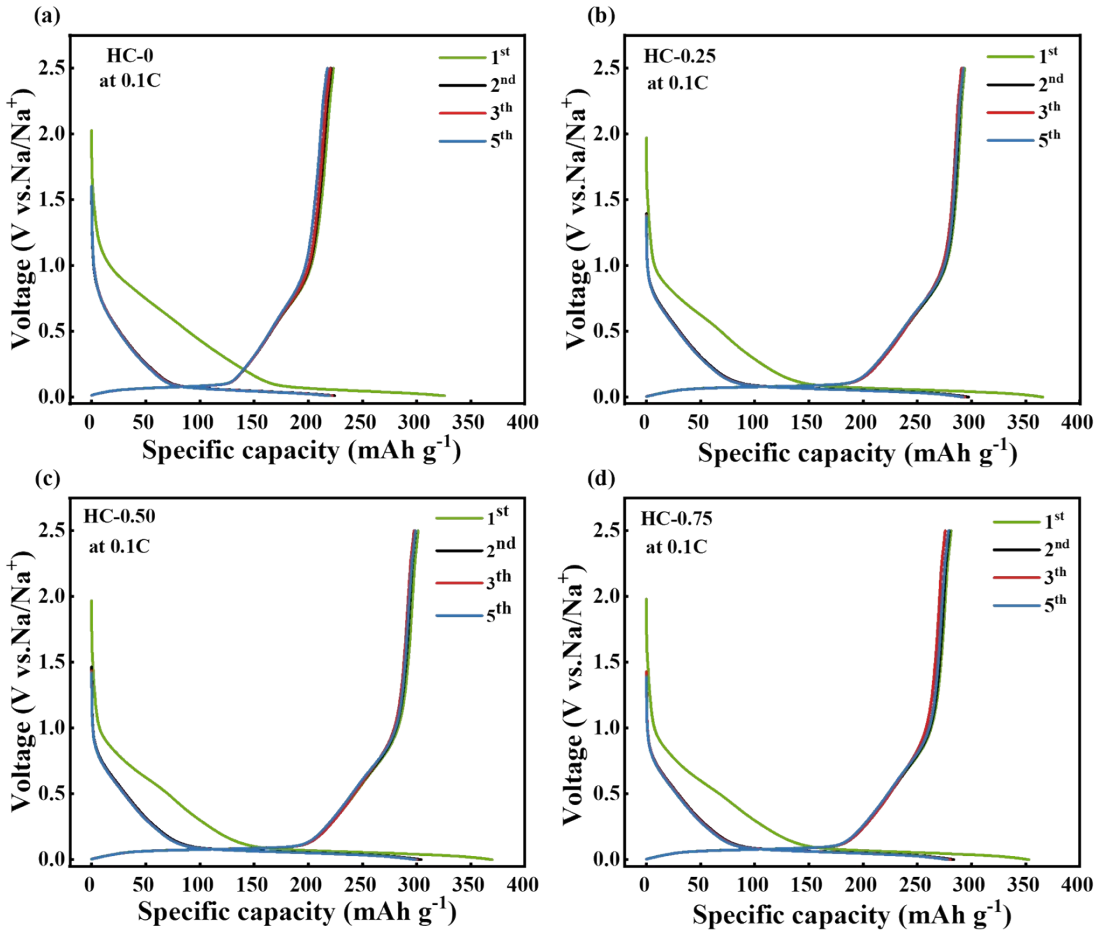

Figure S16. GCD curves of (a) HC-0, (b) HC-0.25, (c) HC-0.50, and (d) HC-0.75 at 1st, 2nd, 3th and 5th cycles.

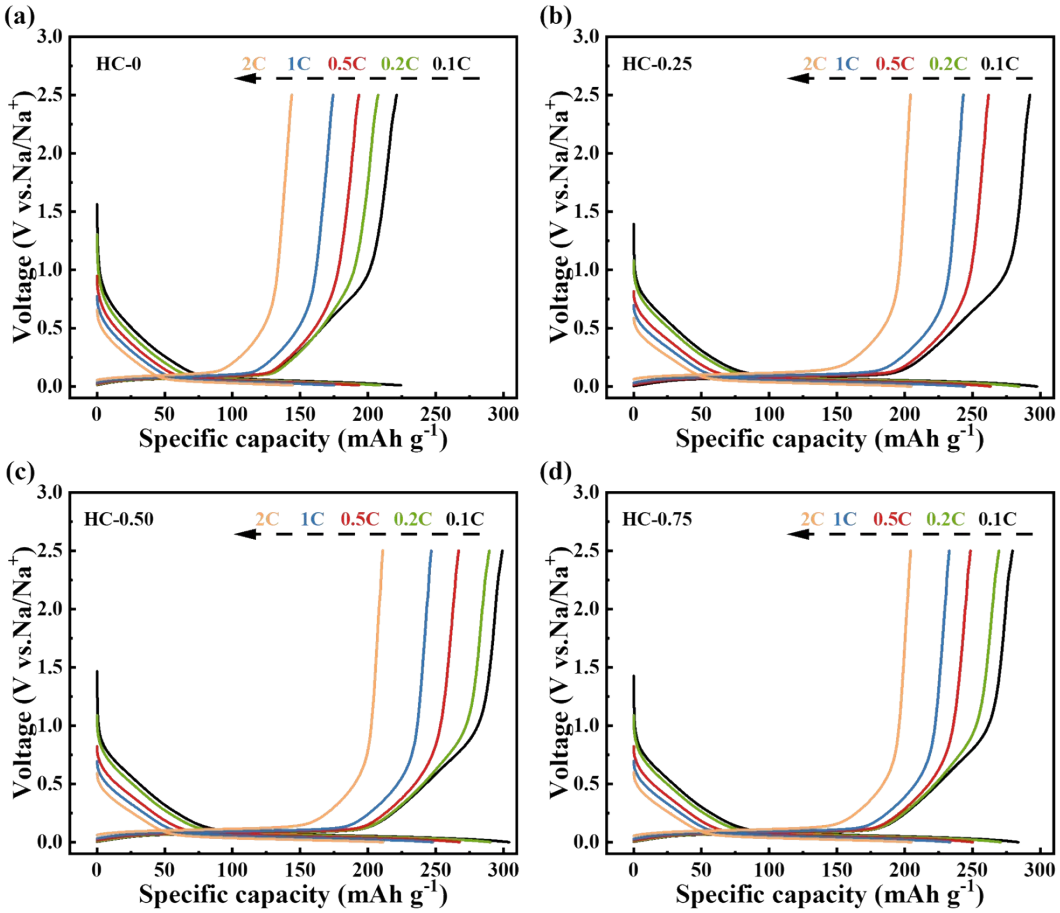

Figure S17. The GCD curves in the potential range for different cycles at 0.1 C, 0.2 C, 0.5 C, 1 C, and 2 C of (a) HC-0, (b) HC-0.25, (c) HC-0.50, and (d) HC-0.75.

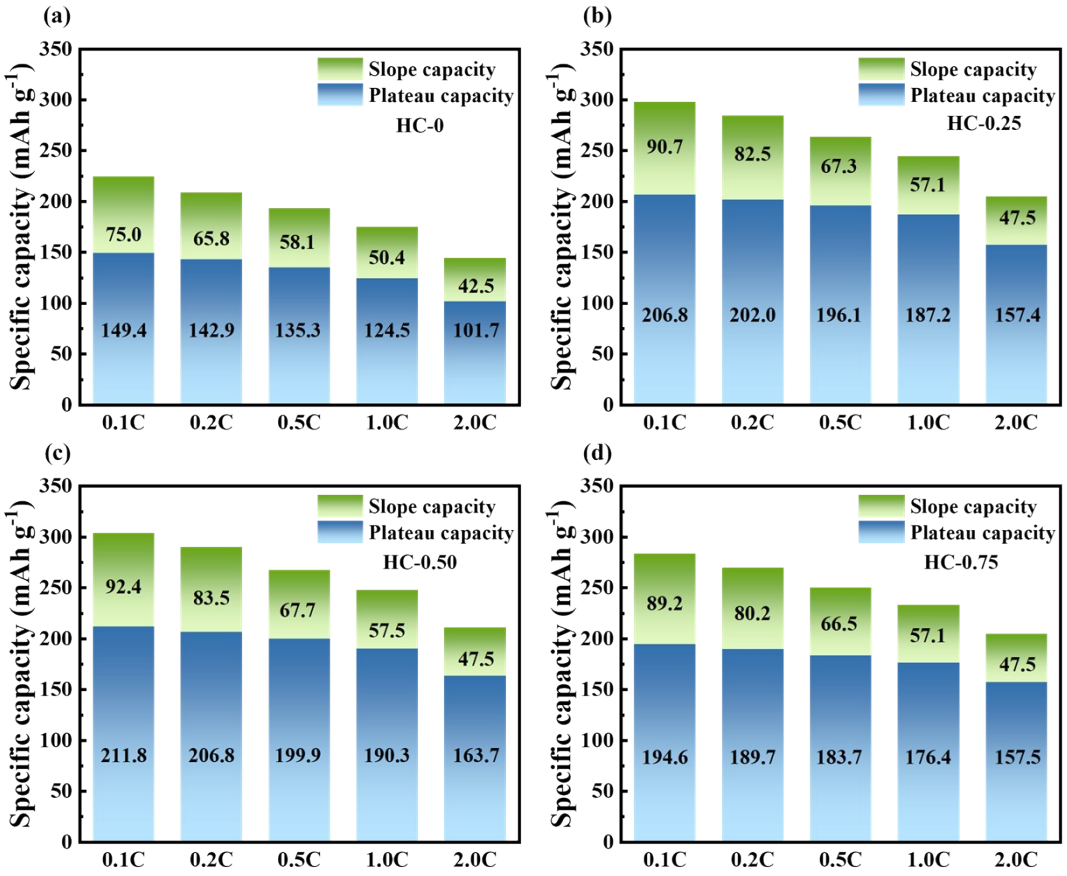

Figure S18. The plateau and slope capacity contribution in the potential range for different cycles at 0.1 C, 0.2 C, 0.5 C, 1C, and 2 C of (a) HC-0, (b) HC-0.25, (c) HC-0.50, and (d) HC-0.75.

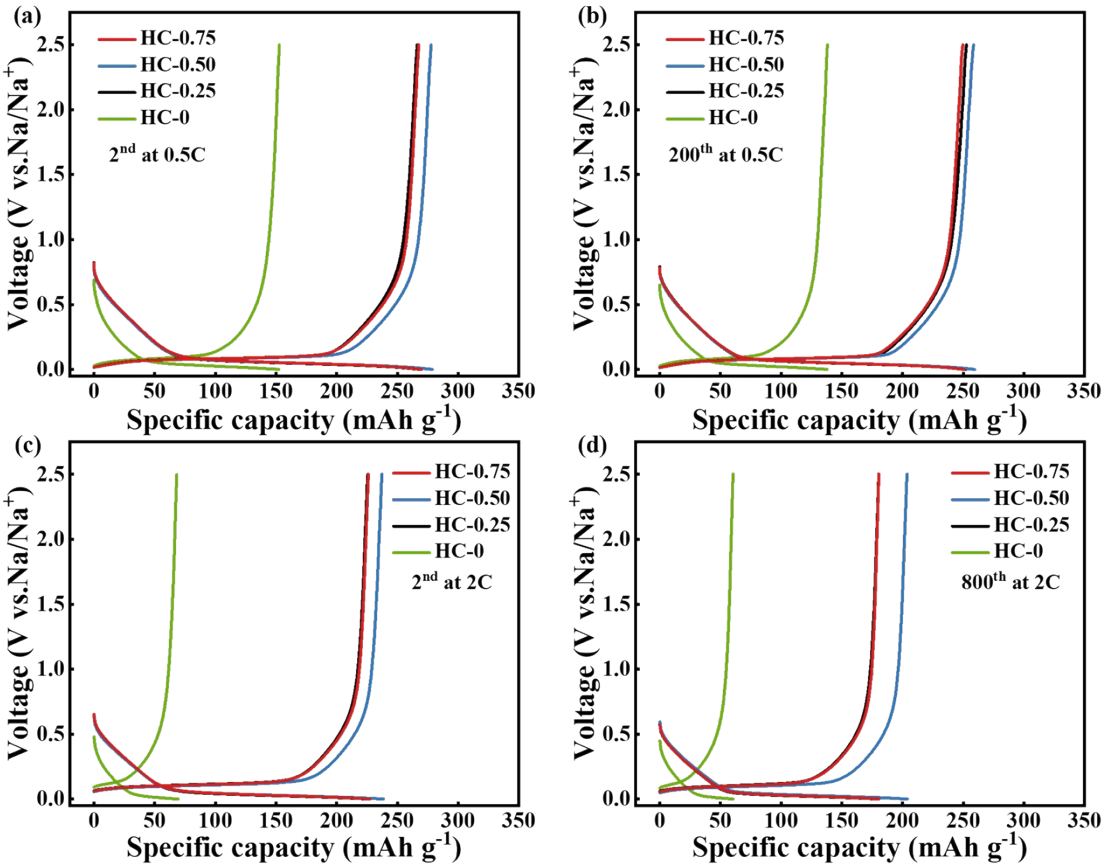

Figure S19. GCD curves at a current density of 0.5 C: (a) in the 2nd cycle, (b) in the 200th cycle. GCD curves at a current density of 2 C (c) in the 2nd cycle, (d) in the 800th cycle.

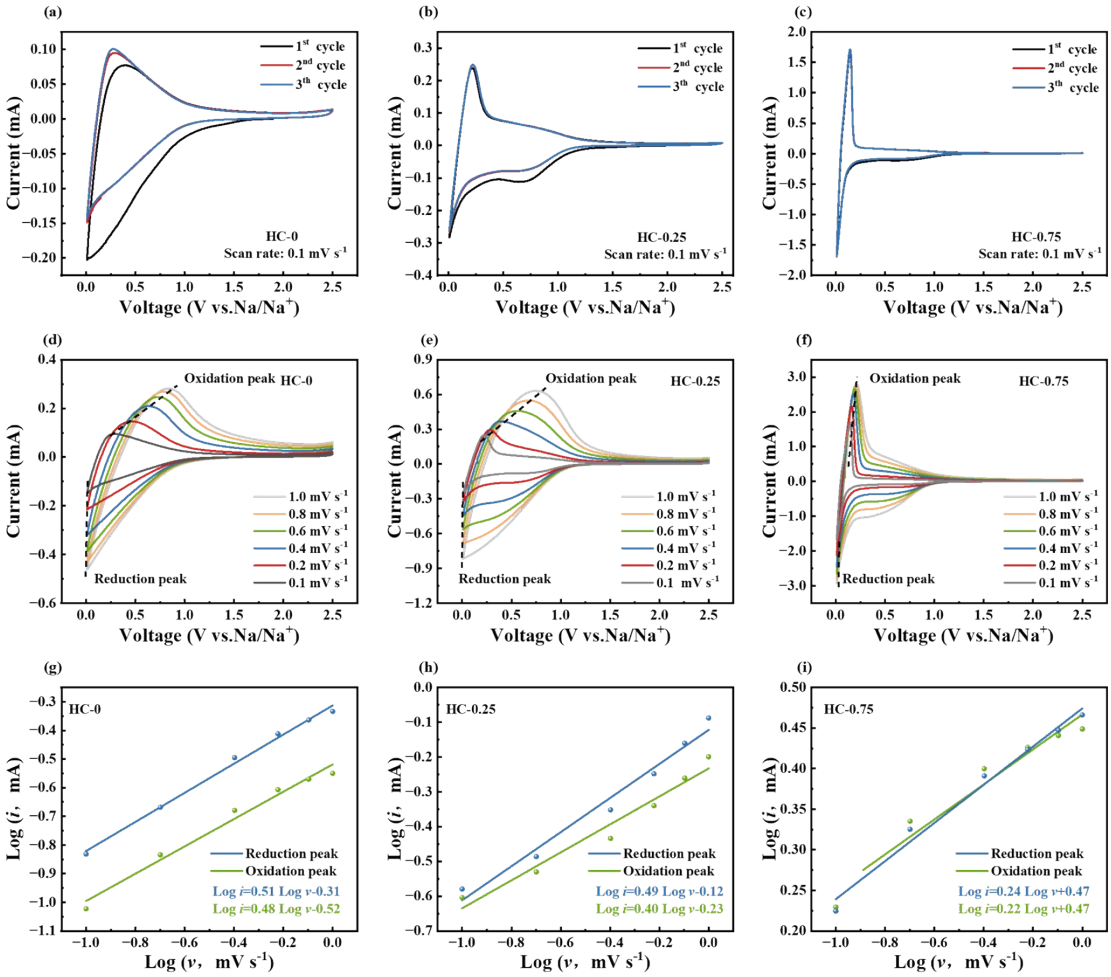

Figure S20. Cyclic voltammograms of the first three cycles at 0.1 mV s^{-1} of (a)HC-0, (b) HC-0.25, and (c) HC-0.75. CV curves under various sweep rates of (d)HC-0, (e) HC-0.25, and (f) HC-0.75. The linear relationship of anodic and cathodic log (peak current) with the log (scan rate) for calculating the exponent (b values) in half cells of (g)HC-0, (h) HC-0.25, and (i) HC-0.75.

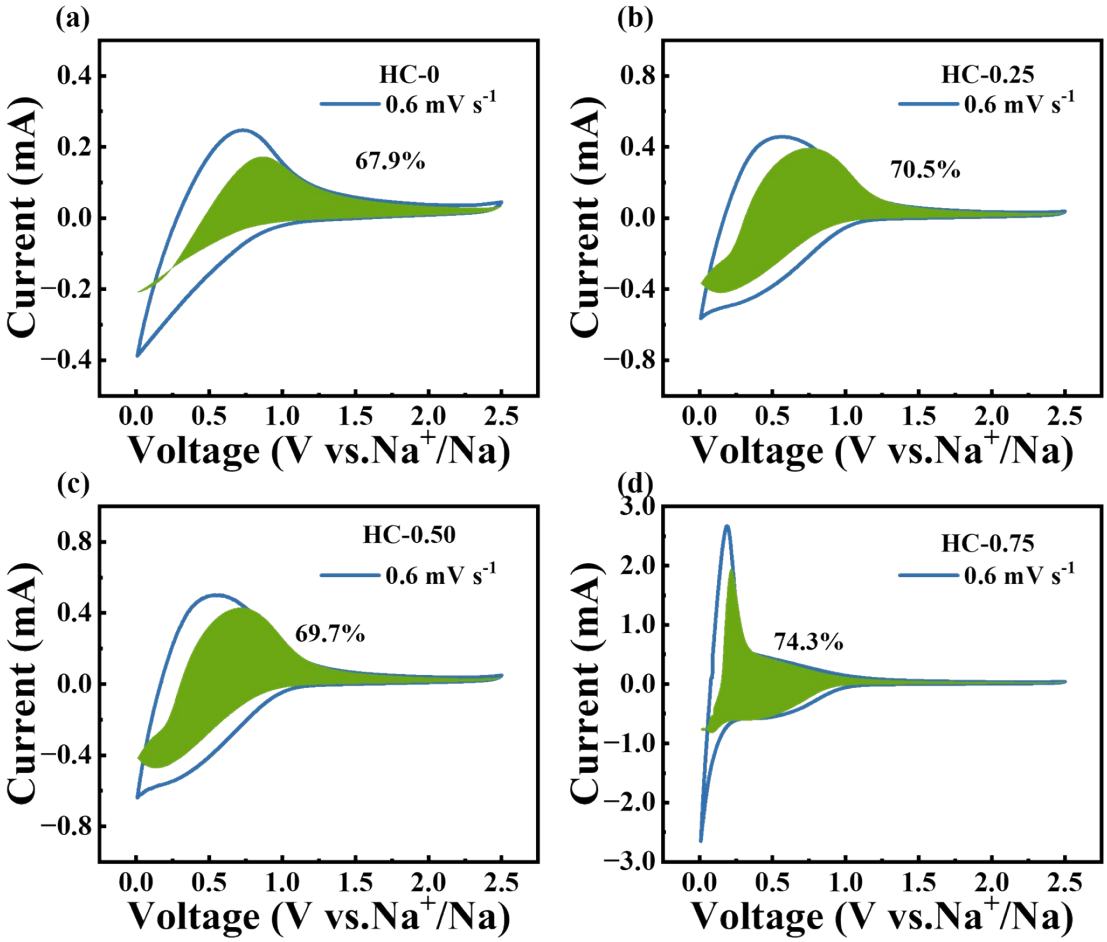

Figure S21. Percentage of pseudo capacitance for scan rate at 0.6 mV s^{-1} of (a) HC-0, (b) HC-0.25, (c) HC-0.50, and (d) HC-0.75

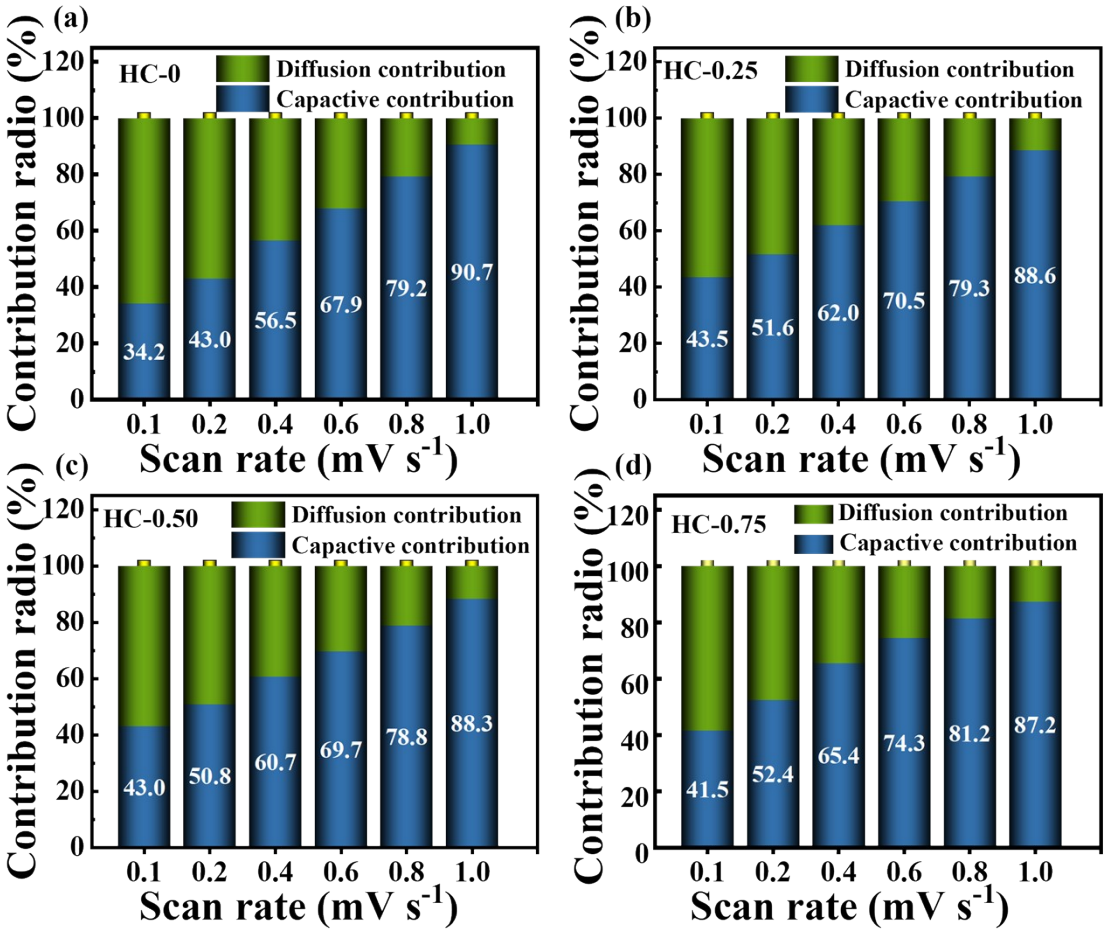

Figure S22. Columns of pseudo capacitance percentage at different scan rates of (a) HC-0, (b) HC-0.25, (c) HC-0.50, and (d) HC-0.75

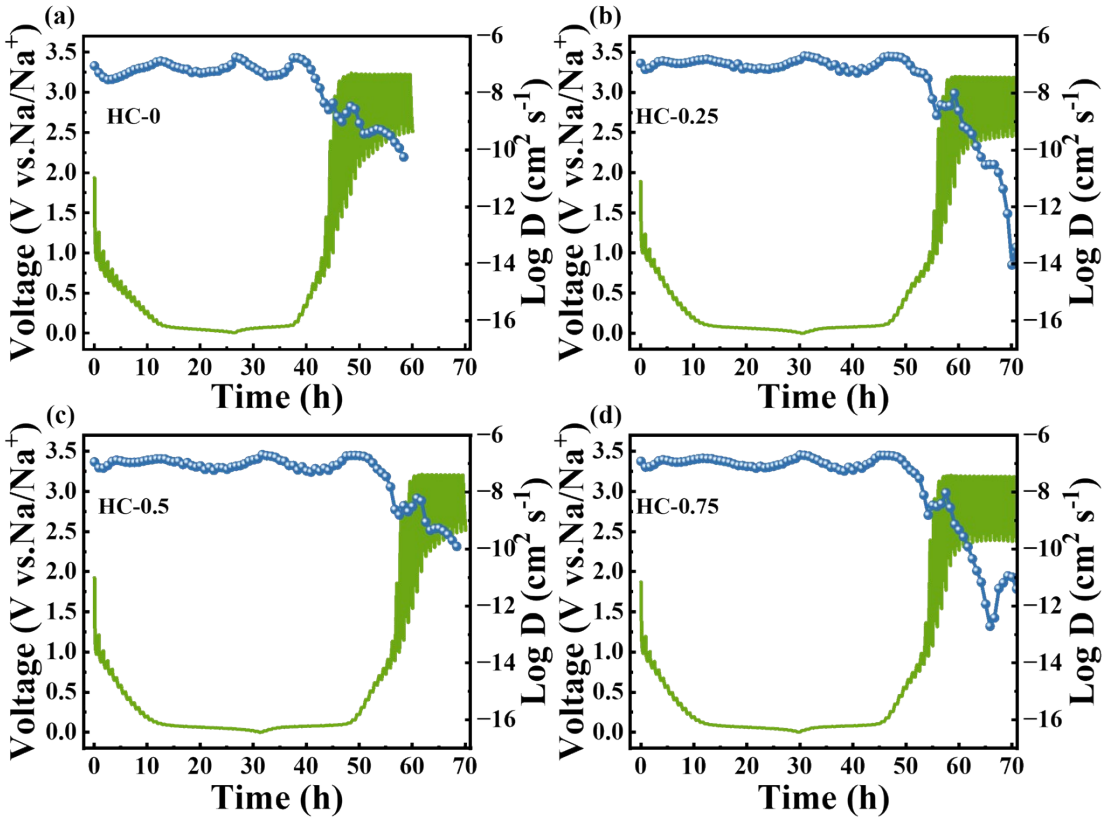

Figure S23. GITT profile, and calculated D_{Na+} (inset) at different voltages with a pulse current of (a) HC-0, (b) HC-0.25, (c) HC-0.50, and (d) HC-0.75.

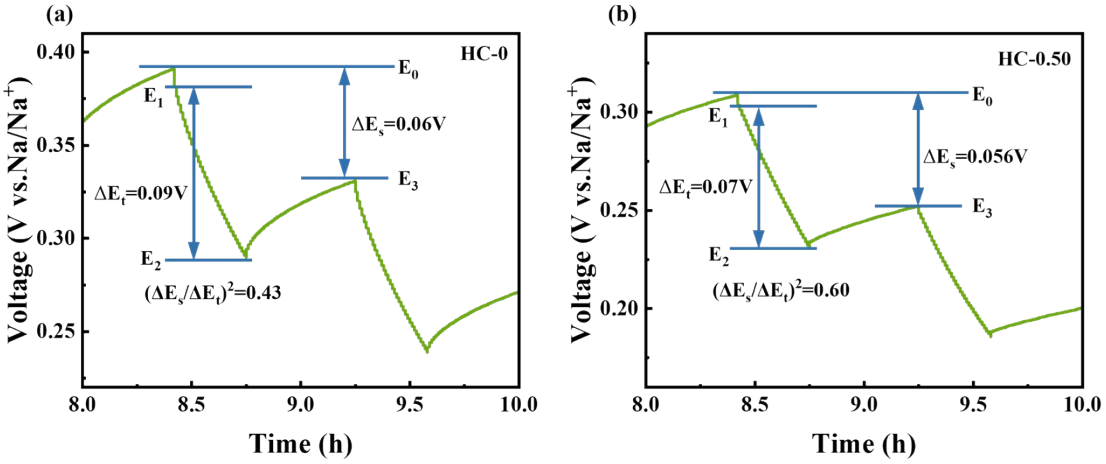

Figure S24. Single-step GITT profile for (a) HC-0, (b) HC-0.50.

Table S1. Physical parameters of the PHC-X samples from XRD.

	PHC-0	**PHC-0.25**	**PHC-0.50**	**PHC-0.75**
I_{002}	20901.6	21435.9	20175.9	19245.3
I_{AM}	16734.2	17268.4	15106.8	14715.0
CrI(%)	19.9	20.4	25.1	23.5

Table S2. The element contents of C and O in HC-X samples.

	HC-0	**HC-0.25**	**HC-0.50**	**HC-0.75**
C(%)	85.02	94.84	94.87	93.66
O(%)	14.98	5.16	5.13	6.34

Table S3. I_D/I_G and L_a values of HC-X samples.

Sample	**I_D/I_G**	**L_a (nm)**
HC-0	0.93	20.7
HC-0.25	1.01	19.0
HC-0.50	1.09	17.6
HC-0.75	0.98	19.6

Table S4. Fitting peak area ratios between D_1, D_3, D_4, and G spectra in the Raman spectrum the different hard carbon materials.

	HC-0	**HC-0.25**	**HC-0.50**	**HC-0.75**
A_{D1}/A_G	1.85	1.86	1.90	1.89
A_{D3}/A_G	1.35	0.78	0.52	0.40
A_{D4}/A_G	0.67	0.42	0.43	0.05

Table S5. The XRD characterizations of the HC-X samples.

Sample	2θ (°)	d_{002} (nm)
HC-0	24.7	0.360
HC-0.25	23.9	0.372
HC-0.50	23.5	0.378
HC-0.75	24.0	0370

Table S6. The BET surface area and pore diameter of the HC-X samples.

Sample	BET surface area (m^2 g^{-1})	D_{BJH}(nm)
HC-0	1.73	19.6
HC-0.25	0.66	29.1
HC-0.50	0.75	29.6
HC-0.75	1.27	21.8

Table S7. Closed pore diameter and volume of the HC-X samples.

Sample	Closed pore diameter (nm)	True density (g m^{-3})	Closed pore volume (cm^3 g^{-1})
HC-0	1.66	2.09	0.036
HC-0.25	1.53	1.73	0.136
HC-0.50	1.63	1.59	0.186
HC-0.75	1.45	1.69	0.149

Table S8. Comparison of electrochemical performance between HC-0.50 and previously reported hard carbon for SIBs.

Sample	Pyrolysis temperature	Current density (mA g^{-1})	Capacity (mAh g^{-1})	ICE (%)	Ref
HC-0.50	**1200℃**	**30**	**304.5**	**81.5**	**This work**
OSHC-1200℃	1200℃	50	286.0	64.5	[11]
VHC-1200	1200℃	25	285.3	75	[12]
HCB1200	1200℃	-	287.0	47	[13]
D-CSHC	1400℃	20	284.5	85.9	[14]
HM-420-6h	1400℃	20	282.9	87.1	[15]
CNA1200	1200℃	50	275	51.53	[16]
CG0.1	1200℃	30	293	84	[17]
PA1200	1200℃	30	222	81	[18]
HC-20	1400℃	20	287.1	76.5	[19]

Table S9. Comparison of electrochemical performance between HC-0.50 and previously reported hard carbon for SIBs after 200 cycles.

Sample	Pyrolysis temperature	Current density (mA g^{-1})	Capacity (mAh g^{-1})	Retention rate (%)	Ref
HC-0.50	**1200℃**	**150**	**260.2**	**92.7**	**This work**
PC-500-1100	1100℃	20	201.0	95.7	[20]
HC-20	1400℃	50	215.4	96.1	[19]
CNA1200	1200℃	100	173.4	91.8	[16]
HCB1200	1200℃	30	246.0	86.0	[13]
FSC	1400℃	100	261.4	-	[21]
CABC-P-2.5	1000℃	60	242.1	90.2	[22]
P-HC	1000℃	100	200.0	-	[23]
SHC-1300	1300℃	50	150.0	82.0	[24]
N-AC-1200	1200℃	100	253.0	-	[25]
HM-420-6h	1400℃	100	180.0	-	[15]
BPHC	1000℃	100	190.0	-	[26]
CHC-2	1000℃	100	247.5	-	[27]

Table S10. Equivalent circuit fitting calculation results of EIS

Sample	R_S (Ω)	R_{ct} (Ω)	D_{Na^+} (cm^2 s^{-1})
HC-0	8.937	9.540	1.23×10^{-12}
HC-0.25	9.646	9.051	1.34×10^{-12}
HC-0.50	8.613	7.162	2.64×10^{-12}
HC-0.75	8.913	7.682	1.84×10^{-12}

References

1. H. Yang, R. Yan, H. Chen, D. H. Lee and C. Zheng, Fuel, 2007, 86, 1781-1788.
2. J. B. Sluiter, R. O. Ruiz, C. J. Scarlata, A. D. Sluiter and D. W. Templeton, Journal of Agricultural and Food Chemistry, 2010, 58, 9043-9053.
3. S. Nam, A. D. French, B. D. Condon and M. Concha, Carbohydrate Polymers, 2016, 135, 1-9.
4. L. Zhu, B. Luo, L. Men, J. Chen, F. Xie, W. Zhang, J. Zhang and Y. Zhou, Green Chemistry, 2025, 27, 2078-2091.
5. Y. Shen, B. Fan, Y. Xin, Q. Zhou, Y. Wang, H. Zhou, K. Zhao, F. Wu and H. Gao, Carbon, 2025, 243, 120594.
6. D. Sun, L. Zhao, P. Sun, K. Zhao, Y. Sun, Q. Zhang, Z. Li, Z. Ma, F. Zheng, Y. Yang, C. Lu, C. Peng, C. Xu, Z. Xiao and X. Ma, Advanced Functional Materials, 2024, 34, 2403642.
7. K. Yu, X. Wang, H. Yang, Y. Bai and C. Wu, Journal of Energy Chemistry, 2021, 55, 499-508.
8. Z. Hou, M. Jiang, Y. Cao, H. Liu, Y. Zhang and J.-G. Wang, Journal of Power Sources, 2022, 541, 231682.
9. Q. Ren, J. Yang, P. Zhang, L. He, Z. Sun, R. Hao and Z. Shi, Advanced Functional Materials, 2025, e25812, 6019-6031.
10. Z. Hou, D. Lei, M. Jiang, Y. Gao, X. Zhang, Y. Zhang and J.-G. Wang, ACS Applied Materials & Interfaces, 2022, 15, 1367-1375.
11. L. Zhou, Y. Cui, P. Niu, L. Ge, R. Zheng, S. Liang and W. Xing, Carbon, 2025, 231, 119733.
12. G. Pan, R. Zhao, Z. Huang, C. Cui, F. Wang, Y. Gu, Y. Gao, Z. Sun and T. Zhang, Carbon, 2024, 224, 118955.
13. S. Sharma, V. Manchala, R. Gopalan, T. N. Rao and B. Das, Carbon, 2024, 226, 119158.
14. Y. Wang, M. Li, Y. Zhang and N. Zhang, Chemical Engineering Journal, 2024, 499, 156115.
15. Y. Lin, J. Jia, J. Wang, X. Kang, G. Huang, B. Xing, W. Kang and C. Zhang, Chemical Engineering Journal, 2025, 504, 158858.
16. H. Wang, H. Niu, K. Shu, L. Sun, Y. Wang, Y. Du, Y. Han, C. Yang and Y.-M. Kang, Journal of Materials Science & Technology, 2025, 209, 161-170.
17. Z. Zhou, Z. Wang and L. Fan, Chemical Engineering Journal, 2024, 490, 151428.
18. Y. Li, Y.-S. Hu, X. Qi, X. Rong, H. Li, X. Huang and L. Chen, Energy Storage Materials, 2016, 5, 191-197.
19. G. Liu, J. Yuan, H. Li, Z. Li, C. Hu, X. Qiao, M. Wang, B. Yuan, P. Zhang and Z. Wu, ACS Applied Materials & Interfaces, 2024, 16, 46226-46236.
20. J. Lan, Q. Lin, X. Li, Y. Cao, H. Chi, M. Li, J. Li, D.-W. Wang and W. Lv, Carbon, 2026, 249, 121220.
21. C. Liu, Y. Pei, X. Wu, N. Zhao, Y. Lv and J. Guo, Carbon, 2025, 243, 120568.
22. Y. Wang, W. Zhang, N. Sun, R. A. Soomro, G. Xu and B. Xu, ACS Applied Materials & Interfaces, 2025, 17, 15436-15445.
23. W. Song, Y. Tang, J. Liu, S. Xiao, Y. Zhang, Y. Gao, C. Yang and L. Liu, Journal of Alloys and Compounds, 2023, 946, 169384.
24. H. Lu, S. Sun, L. Xiao, J. Qian, X. Ai, H. Yang, A.-H. Lu and Y. Cao, ACS Applied Energy Materials, 2019, 2, 729-735.
25. R. Li, B. Yang, A. Hu, B. Zhou, M. Liu, L. Yang, Z. Yan, Y. Fan, Y. Pan, J. Chen, T. Li, K. Li, J. Liu and J. Long, Carbon, 2023, 215, 118489.

26. L. Deng, Y. Tang, J. Liu, Y. Zhang, W. Song, Y. Li and L. Liu, Molecules, 2023, 28, 4921.
27. X.-Y. Wang, K.-Y. Zhang, M.-Y. Su, H.-H. Liu, Z.-Y. Gu, D. Dai, B. Li, J.-W. Wang, X.-Y. He and X.-L. Wu, Carbon, 2024, 229, 119526.